



Simulation of land surface heat fluxes in permafrost regions on the Qinghai-Tibetan Plateau using CMIP5 models

Guojie Hu^a, Lin Zhao^{b,*}, Ren Li^a, Xiaodong Wu^a, Tonghua Wu^a, Xiaofan Zhu^{a,c}, Qiangqiang Pang^a, Guang yue Liu^a, Erji Du^a, Defu Zou^a, Junming Hao^a, Wangping Li^d

^a Cryosphere Research Station on Qinghai-Xizang Plateau, State Key Laboratory of Cryospheric Sciences, Northwest Institute of Eco-Environment and Resources, Chinese Academy of Sciences, Lanzhou 730000, China

^b School of Geographical Sciences, Nanjing University of Information Science & Technology, Nanjing 210000, China

^c University of Chinese Academy of Sciences, Beijing, 100049, China, ^d School of Civil Engineering, Lanzhou University of Technology, Lanzhou, China

^d School of Civil Engineering, Lanzhou University of Technology, Lanzhou, China

ARTICLE INFO

Keywords:

Land surface heat flux
Freezing and thawing process
Permafrost
Qinghai-Tibetan Plateau

ABSTRACT

The variations in land surface heat fluxes affect the ecological environment, hydrological processes and the stability of surface engineering structures in permafrost regions of the Qinghai-Tibetan Plateau (QTP). Based on observation data from a meteorological station in the Tanggula site in 2005, which is located in a permafrost region on the QTP, the performances of seventeen selected the phase 5 of the Coupled Model Intercomparison Project (CMIP5) were evaluated. The results showed that these simulations did not perform well using sensible heat flux, downward shortwave radiation or upward shortwave radiation, and differences exist among the models. The average multimodel ensemble results were similar to the observed land surface heat fluxes. The results revealed that the monthly average latent heat flux and the net radiation were small in December and January and large in May, June and July. The fluctuation in the soil heat flux was well correlated with the net radiation, and the sensible heat flux was negative in January and December in northwest of the Plateau. The latent heat flux was the strongest over the southeastern QTP from May to August, and it decreased over the northwestern QTP. In contrast, the sensible heat flux was the weakest over the southeastern QTP, and it gradually increased and became dominant over the northwestern QTP. The results also indicated that there was a good correlation between the surface heating field intensity and the net radiation, with a correlation coefficient of 0.99; this indicates stronger heating over the eastern QTP than over the western QTP and stronger heating over the southern QTP than over the northern QTP. Furthermore, the Bowen ratio was higher during the freezing and thawing stages than that during the completely thawed stage. This ratio was larger over the central and northeastern QTP and smaller along the northwest edge of the QTP, which was lower (range from -0.81 to 4.86) due to the overestimation of precipitation, a smaller difference between the simulated monthly average surface temperature and the observed air temperature, and a decrease in wind speed when using the CMIP5 models in the permafrost region of the QTP. This research provides a foundation for understanding land surface heat flux characteristics in the permafrost regions on the QTP under climate change.

1. Introduction

The Qinghai-Tibetan Plateau (QTP), also referred to as the “Third Pole of the Earth”, exerts a profound impact on both local weather and global climate (Han et al., 2017; Yanai and Wu, 2006; Ye and Gao, 1979). Due to its terrain, the surface of the QTP receives large amounts of solar radiation and undergoes unusual seasonal changes in land surface heat and water fluxes (Ma and Ma, 2016). The energy and water cycles play important roles in the Asian Monsoon system over the QTP

(Ma et al., 2011; Qiu, 2008; Yanai et al., 1992); the thermodynamic processes over the QTP may impact the climate at the hemispheric scale and even the global scale through the modulation of atmosphere-ocean interactions (Ma et al., 2011; Qiu, 2008; Yanai et al., 1992; You et al., 2017; Zhao et al., 2000; Zhou and Huang, 2012; Zhou et al., 2009). In recent years, there have been several published studies on land surface heat fluxes over the QTP (Han et al., 2017; Kang et al., 2010; Ma et al., 2011; Ma et al., 2006; Yang et al., 2003; You et al., 2016). However, the changes in land surface heat fluxes over the QTP still have large

* Corresponding author.

E-mail addresses: huguojie123@lzb.ac.cn (G. Hu), linzhao@lzb.ac.cn (L. Zhao).

<https://doi.org/10.1016/j.atmosres.2019.01.006>

Received 19 March 2018; Received in revised form 27 December 2018; Accepted 7 January 2019

Available online 09 January 2019

0169-8095/ © 2019 Elsevier B.V. All rights reserved.

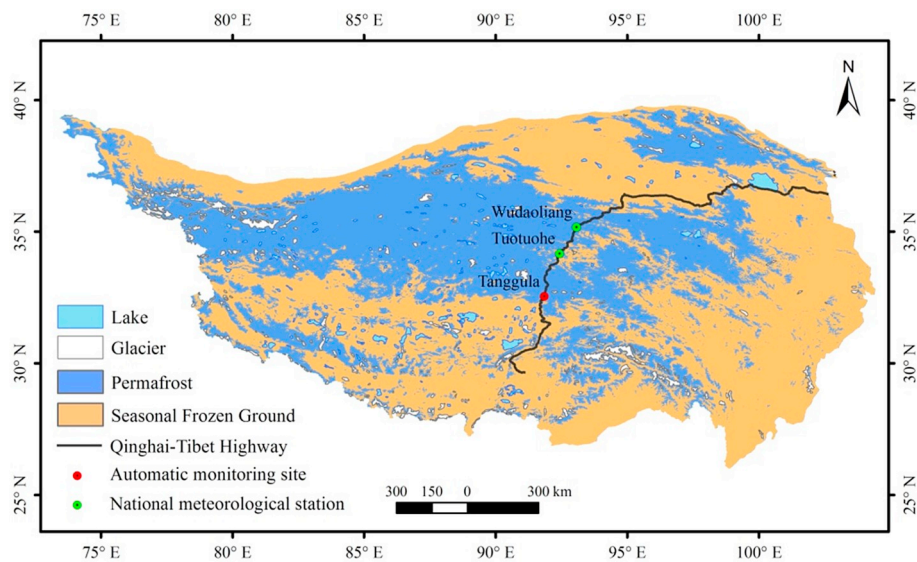


Fig. 1. Map of the frozen ground and the locations of selected comprehensive observation and national meteorological stations on the Qinghai-Tibetan Plateau in China.

Table 1
CMIP5 models used in this study.

Model name	Modeling groups	Resolution
ACCESS1-0	Commonwealth Scientific and Industrial Research Organization (CSIRO) and Bureau of Meteorology (BOM), Australia	1.88° × 1.24°
ACCESS1-3		1.88° × 1.24°
CCSM4	National Center for Atmospheric Research	1.25° × 0.94°
CMCC-CM		0.75° × 0.75°
CMCC-CMS	Centro Euro-Mediterraneo per I Cambiamenti Climatici	1.88° × 1.88°
CNRM-CM5		1.41° × 1.41°
CSIRO-Mk3.6.0	Centre National de Recherches Meteorologiques/Centre Europeen de Recherche et Formation Avancees en Calcul Scientifique	1.88° × 1.88°
HadGEM2-CC		1.88° × 1.24°
HadGEM2-ES	Commonwealth Scientific and Industrial Research Organization in collaboration with Queensland Climate Change Centre of Excellence	1.88° × 1.24°
inmcm4		2.00° × 1.50°
MIROC4h	Institute for Numerical Mathematics	0.56° × 0.56°
MIROC5		1.41° × 1.41°
MPI-ESM-LR	Atmosphere and Ocean Research Institute (The University of Tokyo), National Institute for Environmental Studies, and Japan Agency for	1.88° × 1.88°
MPI-ESM-MR		1.88° × 1.88°
MPI-ESM-P	Marine-Earth Science and Technology	1.88° × 1.88°
MRI-CGCM3		1.13° × 1.13°
MRI-ESM1	Max Planck Institute for Meteorology	1.13° × 1.13°
		1.13° × 1.13°

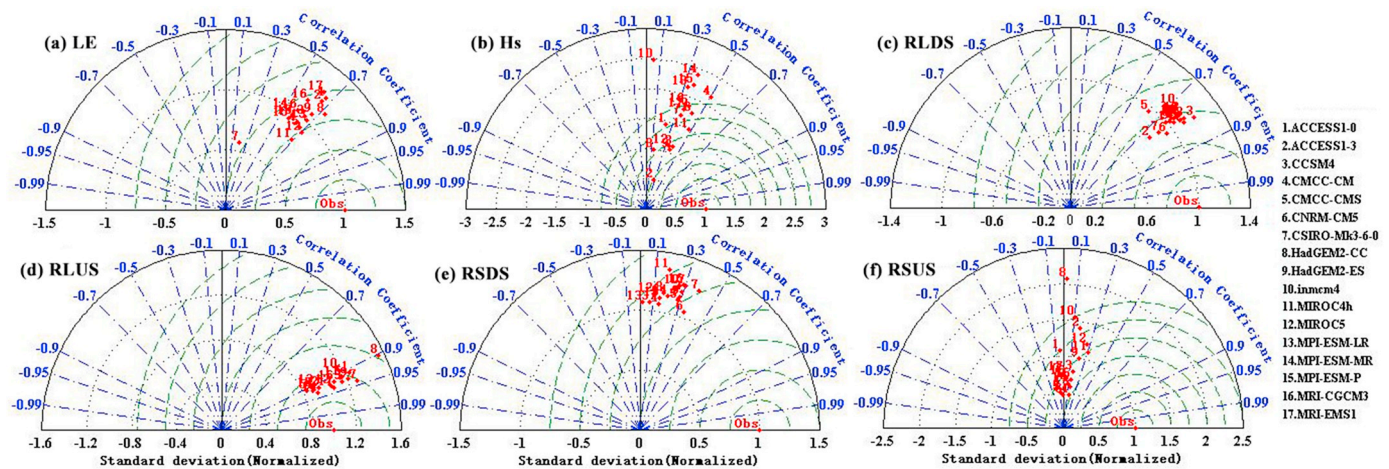


Fig. 2. Taylor program for daily averages of the surface energy fluxes of LE, Hs, RLDS, RLUS, RSDS and RSUS between CMIP5 models and observation at Tanggula site in 2005.

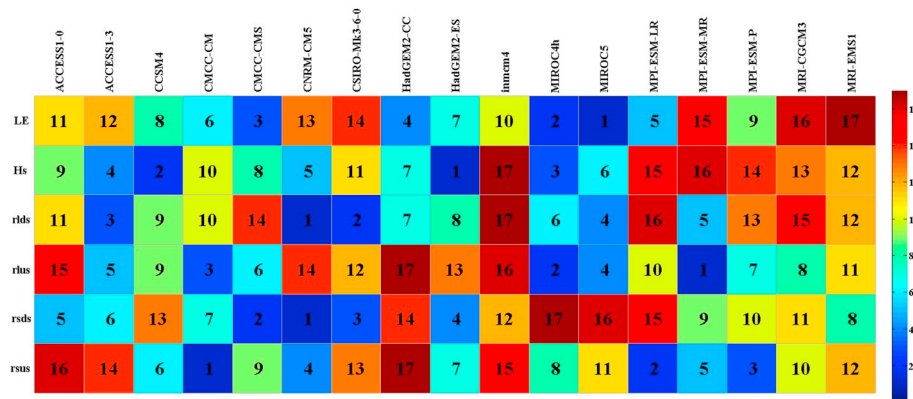


Fig. 3. The portrait diagram of the models rank based on composite rating indicator for the surface energy fluxes of all indices at Tanggula site in 2005.

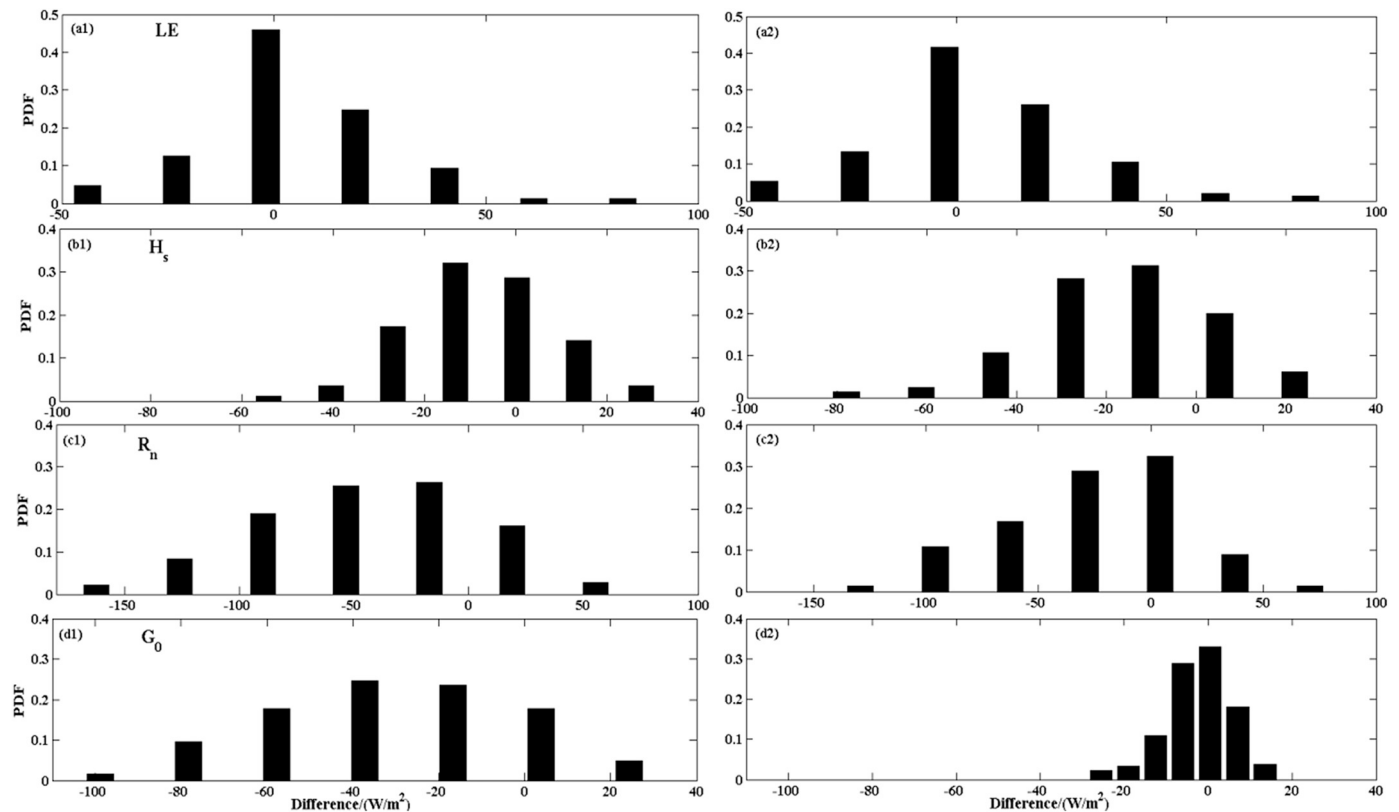


Fig. 4. The probability distribution function (PDF) of the difference between the modeled and observed land surface heat flux by the best multi-models ensemble ((a1)~(d1)) and the average multi-model ensemble ((a2)~(d2)).

uncertainties, such as seasonal variations in land surface heat flux was more complicated, mismatch in spatial representation between estimated fluxes and in situ observations, topographical differences and parameterization schemes (Han et al., 2017; Yang et al., 2014), especially regarding surface sensible heat flux and the energy balance in permafrost regions of the QTP (Han et al., 2017; Yao et al., 2011). Therefore, these findings have highlighted the necessity to investigate the characteristics of land surface heat fluxes on the QTP, which play critical roles in understanding regional and global climate change (Han et al., 2017).

The permafrost of the QTP covers approximately 1.06 million km² and accounts for 42.4% of the total area (Zou et al., 2017), which is the largest permafrost and thickest active layer in the middle and low latitudes (Xiao et al., 2011). This permafrost is much warmer than that in

circumpolar regions; thus, it is the most sensitive to climate change, indicating that the QTP has become the first detected area to be impacted by climate change (Cheng, 1990; Liu and Chen, 2000; Tang et al., 1979). The seasonal freeze-thaw cycle is the most influential physical characteristic in the active layer of permafrost regions on the QTP, as it changes soil thermal properties, surface albedo, surface evaporation, and vegetation conditions and leads to the redistribution of energy and water between the soil and the atmosphere (Chen et al., 2014a; Zhang et al., 2016). Previous studies have noted that the soil freezing and thawing process plays an important role in the transition from the dry-season to the wet-season, and it effects the circulation over East Asia, the summer precipitation in China and the outbreak of the east Asian summer monsoon (Guo et al., 2009; Wang and Shang, 2007). Surface energy exchanges mainly occur through the interaction

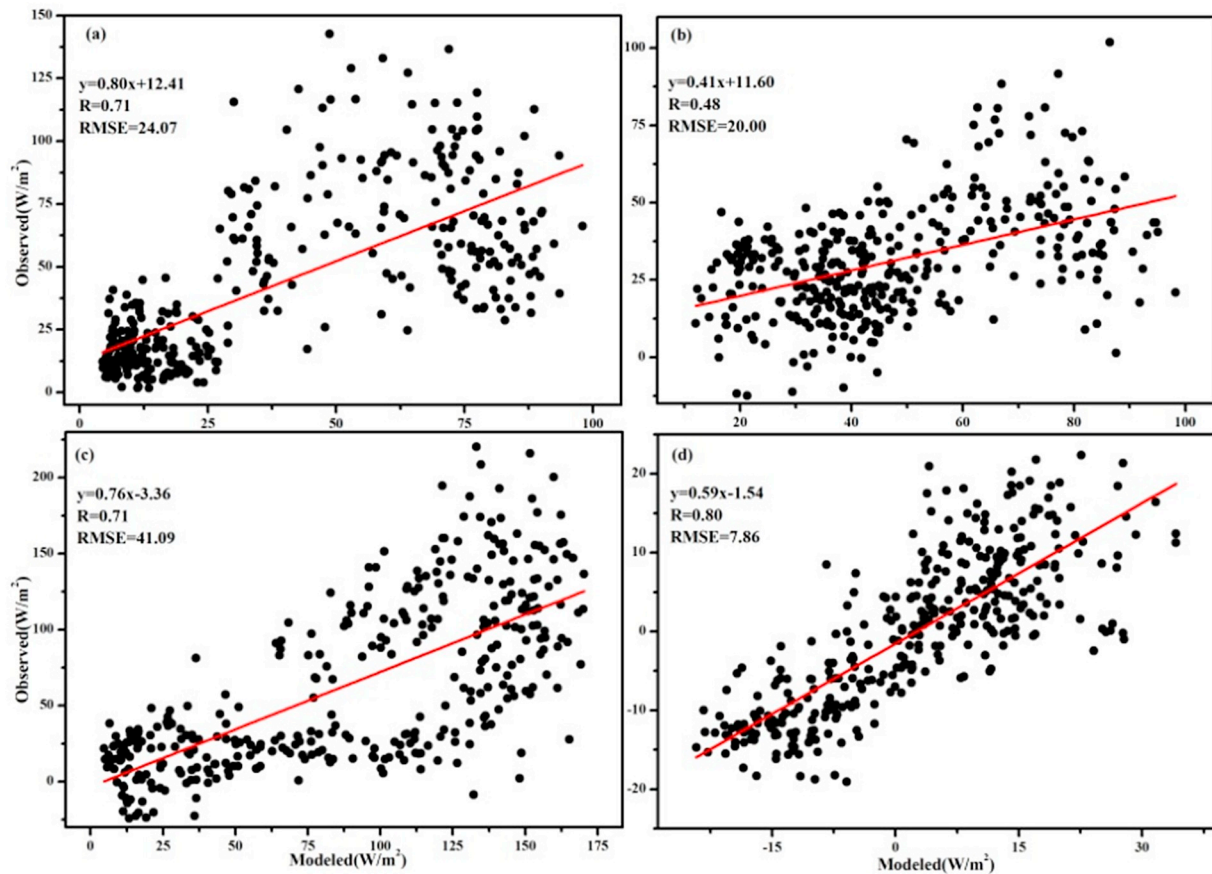


Fig. 5. Land surface heat flux simulated by the average multi-model ensemble vs. observed: (a) latent heat flux, (b) sensible heat flux, (c) net radiation heat flux and (d) soil surface heat flux at Tanggula site in 2005.

between surface heat fluxes and radiation balance changes, and the response of the land surface system to climate change is also transmitted through the processes of surface heat and radiation balance. In recent years, precipitation, air temperature, and ground temperature change trends have drastically increased in permafrost regions of the QTP (Hu et al., 2019; Zhao et al., 2010; Zhu et al., 2011). Thus, the change in land surface heat fluxes in permafrost regions on the QTP have received more attention (Li et al., 2007). Several studies have documented the land surface heat fluxes in the permafrost regions of the QTP; they mainly focused on the northern QTP and a single point (Ma et al., 2005). The results of these studies indicate that the surface energy balance has obvious seasonal variations and regional differences, and precipitation, freezing and thawing processes in the active layer that are caused by monsoons have great impacts on the surface energy balance (Yao et al., 2011; Zhang et al., 2016). However, these studies were based on points or specific localities in the permafrost on the QTP. Numerical models, combined with in situ observation data, were the main tools utilized to simulate regional land surface heat fluxes over inhomogeneous land surface features (Ma and Ma, 2016; Zhou and Du, 2016). Therefore, further understanding land surface heat flux characteristics in these regions has important implications for climatological and hydrological changes, especially for land-atmosphere interactions.

However, there are 80 meteorological stations mainly located in the central and eastern QTP and very few monitoring stations western QTP because of the harsh environment (Han et al., 2017; Hu et al., 2016; Yin et al., 2013), especially for acquiring high space-time resolution observation data in permafrost regions, which makes research work on the

permafrost very difficult (Chang et al., 2016). The numerical model is an important tool for studying land-atmosphere interactions in the permafrost regions of the QTP. Nonetheless, many climate models just provide approximations of the actual weather and climate system (Zeng et al., 1989); therefore, it is necessary to carry out an evaluation to improve climate model effectiveness and objectively evaluate the reliability and uncertainty of the simulation results. The framework for phase 5 of the Coupled Model Intercomparison Project (CMIP5) represents the latest and most ambitious coordinated international climate model intercomparison exercise (Taylor et al., 2012). However, little is known about the performance of land surface heat flux when using CMIP5 in the permafrost regions of the QTP. Meanwhile, because of the complexity of the east Asian monsoon system and the complex terrain of the QTP, the simulation of weather patterns still has deficiencies, such as the simulation of surface air temperature (e.g., the overestimation of cold temperatures) and the overestimation of precipitation, especially when the model error is amplified over the QTP (Hu et al., 2014; Jiang et al., 2017; Wang and Xiong, 2004; Zhou and Du, 2016). Additionally, a detailed description of the land surface is needed for the permafrost regions on the QTP (Wang and Shi, 2007). However, there are still few studies on the effects of the freeze-thaw process on regional climate. Because more multiscale complexities exist in the nonlinear interactions of the climate system, the resolution of climate system models is limited, and the parameterized scheme has discrepancies, which results in a climate system model with many uncertainties (Chang et al., 2016). In addition, changes in the active layers of permafrost regions cause complexities in the QTP, which has also led to great uncertainties in surface energy exchange (Li et al., 2011).

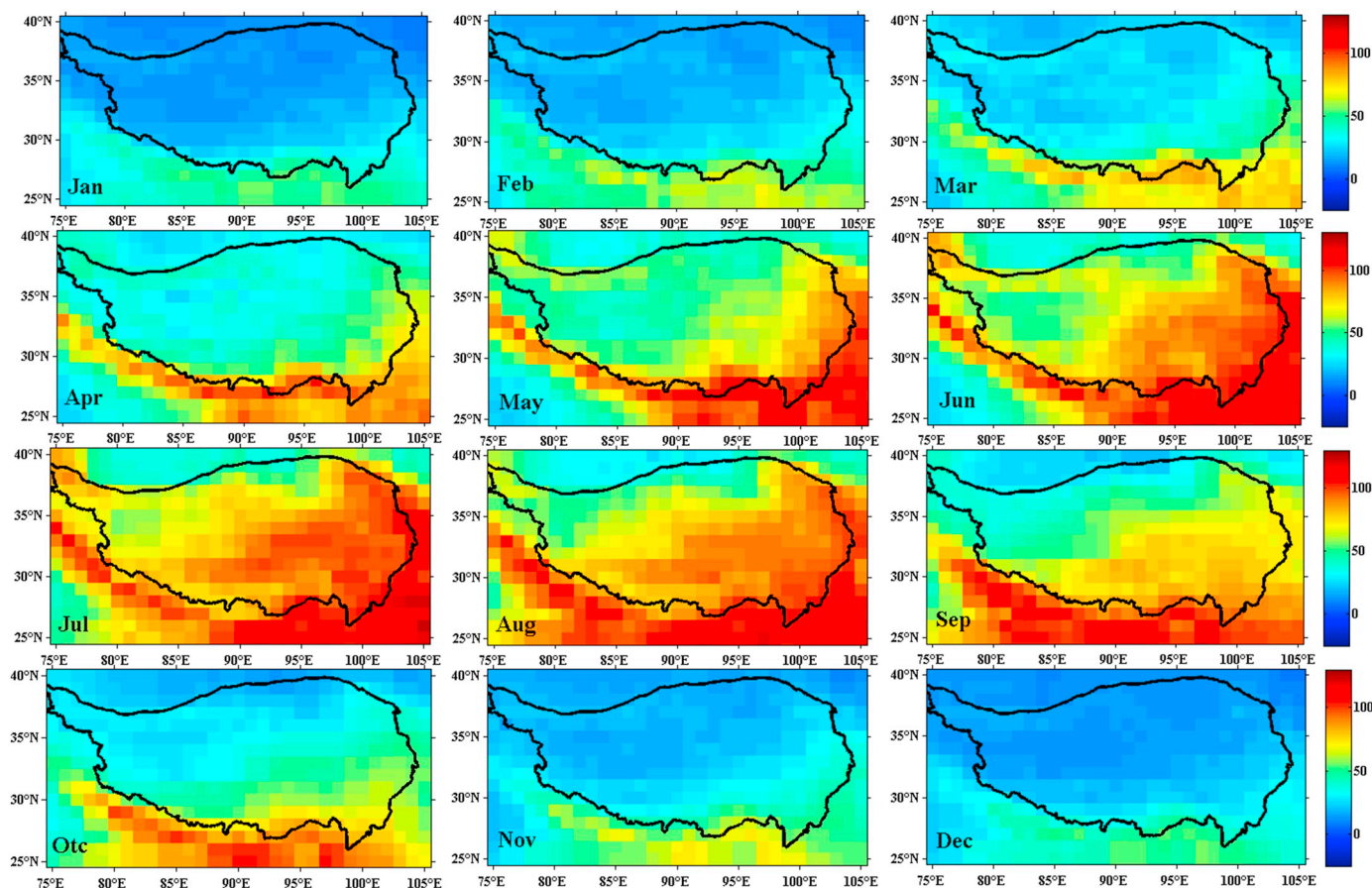


Fig. 6. The monthly average of latent heat flux over the QTP from the 17 CMIP5 models along with their ensemble mean in 2005. (units: W/m^2).

Meanwhile, there is still little known regarding land surface heat fluxes at the regional scale in permafrost regions on the QTP (Li et al., 2012). Therefore, evaluating the use of CMIP5 models when analyzing land surface heat fluxes in permafrost regions on the QTP is necessary, and the objectives of this study are to (1) evaluate the performance of the CMIP5 model simulation on land surface heat fluxes in the permafrost regions of the QTP; (2) analyze variations in the spatial distribution of land surface heat flux values on the QTP; (3) demonstrate the effect of the freezing and thawing process on land surface heat fluxes in the permafrost regions of the QTP.

2. Data and methods

2.1. Data

With an altitude of 5100 m, the studied Tanggula site (33.07°N and 91.93°E) is situated on a gentle slope at the Tanggula Mountains on the QTP in China. The monitoring site (Fig. 1) is located in the continuous permafrost zone, and the underlying surface belongs to an alpine meadow (Hu et al., 2015; Yao et al., 2008). The observation site was established in June 2004. The hourly meteorological data, consisting of precipitation, global radiation, net radiation, air temperature, wind speed and relative humidity measurements, were recorded using a CR23X data acquisition instrument (Campbell Scientific Inc.). The air temperature, relative humidity, and wind speed were measured at heights of 2 and 10 m. The snow depth was measured by SR50 snow depth instrument (Campbell, USA). The data used in this study are the daily and monthly average values in 2005. Meanwhile, two national meteorological stations distribute in permafrost regions were selected,

which were Tuotuohe (34.13°N and 92.26°E) and Wudaoliang (35.13°N and 93.05°E), with an altitude of 4533 m and 4612 m, respectively (Fig. 1). The data of monthly average air temperature, precipitation, wind speed and surface temperature in 2005 are provided by National Meteorological Information Center (NMIC), China Meteorological Administration (CMA) (available at <http://data.cma.gov.cn>).

The 17 models from CMIP5 Project used in this study are listed in Table 1, together with their modeling groups, their abbreviations and resolution as used in this manuscript. Further model details and information on their configuration or features can be found in the Program for Climate Model Diagnosis and Intercomparison (PCMDI) data portal (<http://www.pcmdi.llnl.gov/>) (Taylor et al., 2012). The model land surface heat fluxes analyzed in this study are taken from the “historical” experiments covering 2005 are selected and interpolated to a common $1.0 \times 1.0^\circ$ grid using a nearest interpolation procedure.

2.2. Method

The net radiation (R_n) was calculated using data from four radiation components according to the following equation:

$$R_n = RS_{DS} - RS_{US} + RL_{DS} - RL_{US} \quad (1)$$

where RS_{US} is the upward short-wave radiation (W/m^2), RS_{DS} is the downward short-wave radiation (W/m^2), RL_{US} is the upward long-wave radiation (W/m^2), and RL_{DS} is the downward long-wave radiation (W/m^2).

The sensible heat flux (H_s) and latent heat flux (LE) were calculated via the eddy covariance method every 30 min using the observation data from the eddy covariance system at Tanggula site (Gu et al., 2015).

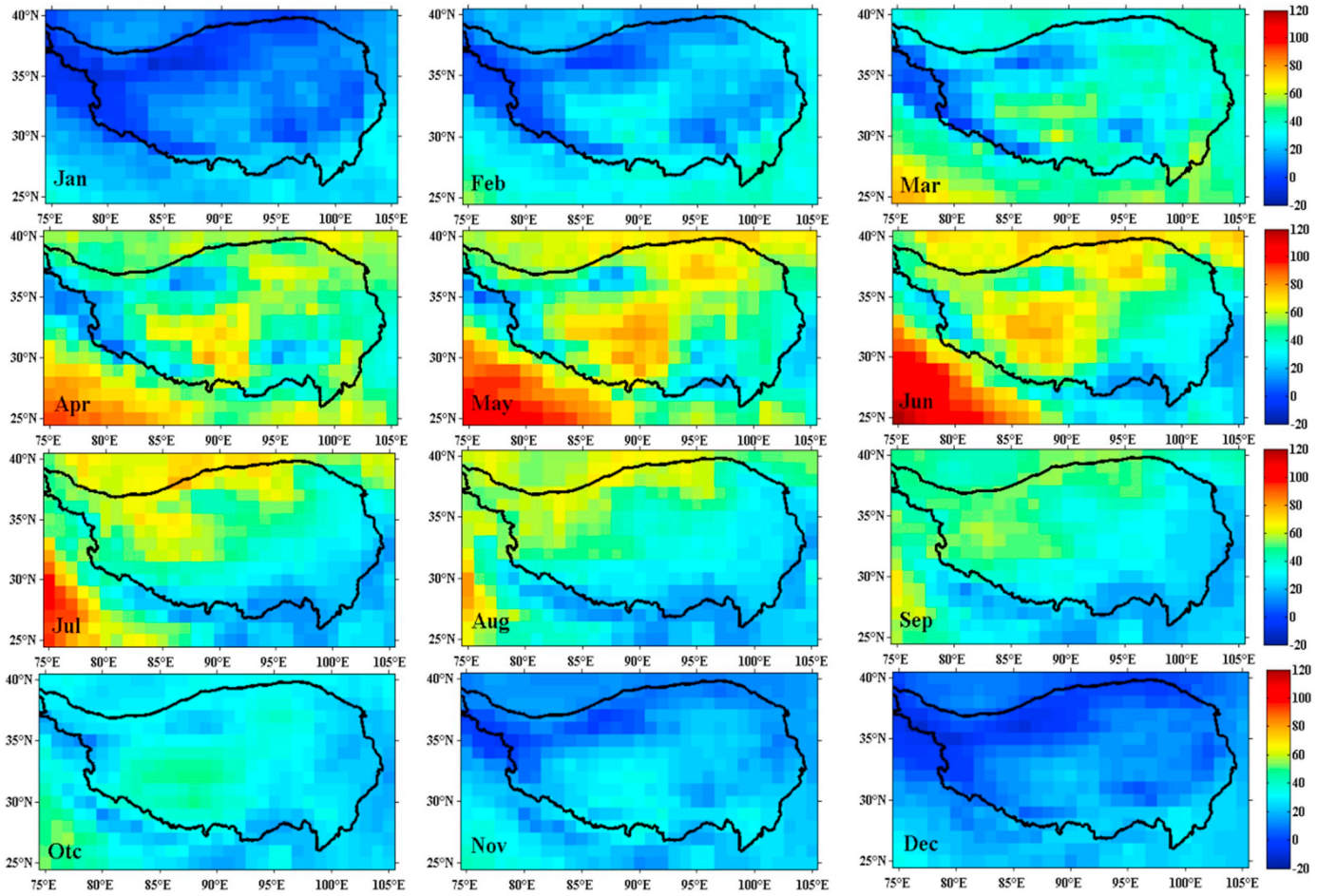


Fig. 7. The same as Fig. 6, but for sensible heat flux.

For CMIP5 models, the ground heat flux (G_0) was calculated according to the

$$G_0 = R_n - LE - H_s \quad (2)$$

where H_s is surface sensible heat flux; and LE is surface latent heat flux.

The ground heat flux (G_0) was calculated according to Tanaka et al. (2003) with the observed soil heat flux at 10 cm at Tanggula site (Gu et al., 2015).

In addition, 17 CMIP5 model simulations of 3 indices are chosen, and the root-mean-square error, the standard deviations and correlation between the model and observation are calculated. The comprehensive model rank (M_R) (Jiang et al., 2017; You et al., 2018) which measures the consistency of simulations for each model is defined as:

$$M_R = 1 - \frac{1}{1 \times m \times n} \sum_{i=1}^n \text{rank}_i \quad (3)$$

where m and n is the number of models and indices, and rank_i is based on model's order of performance on each index. The M_R of the best-performing model is closer to 1, indicating higher skill (You et al., 2018).

3. Results

3.1. CMIP5 model performance for surface energy fluxes in permafrost regions

3.1.1. Evaluation of temporal variability in permafrost regions

Fig. 2 shows the daily surface energy fluxes in the permafrost regions at the Tanggula site in 2005 from the 17 CMIP5 models. It can be

seen that all of the models have good simulation ability for LE , $RLDS$ and $RLUS$. The correlation coefficient of the simulation for LE between the modeled and the observation values is approximately 0.7, except for CSIRO-MK3-6-0. The RMSE of the simulation for $RLUS$ is < 1.5 for most of the models, except for HadGEM2-CC. Different models have good consistency in the simulation of LE , $RLDS$ and $RLUS$, and the distributions are shown to be concentrated via a Taylor diagram. In addition, it is necessary to note that the standard deviations values of the simulations for H_s and $RSDS$ are greater than those for the observations in most of the models and for the simulation of $RSUS$ in half of the models. The correlation coefficients of all the models are lower than 0.50 for H_s , $RSDS$ and $RSUS$. The results also reveal that the simulation ability for each model is substantially different when examining H_s , which has a correlation coefficient < 0.50 for all models, a standard deviation > 1.5 for most of the models, and a RMSE > 1.5 . The standard deviation ratio of several models is > 1.0 for $RSUS$ (RMSE > 1.0), and the correlation coefficients of several models are even < 0 .

To synthesize the three assessment indices, an M_R value is calculated for each model to illustrate their overall ranking regarding daily surface energy fluxes in permafrost regions at the Tanggula site in 2005 (Fig. 3). Each model is ranked from 1 (best) to 17 (worst) for each index. The length of the colored columns summarizes each ranking, where shorter columns indicate a better model performance. The colors represent the ranking of each individual index. The models have large differences in simulation ability for each index. It is found that MIROC5, MIROC4h, CMCC-CMS, HadGEM2-CC, MPI-ESM-LR, HadGEM2-ES, CCSM4, MIROC4h, ACCESS1-3 and CNRM_CM5 possess the best skills for simulating LE and H_s . The poorest performances are found using HadGEM2-CC, ACCESS1-0 and INMCM4 for simulating

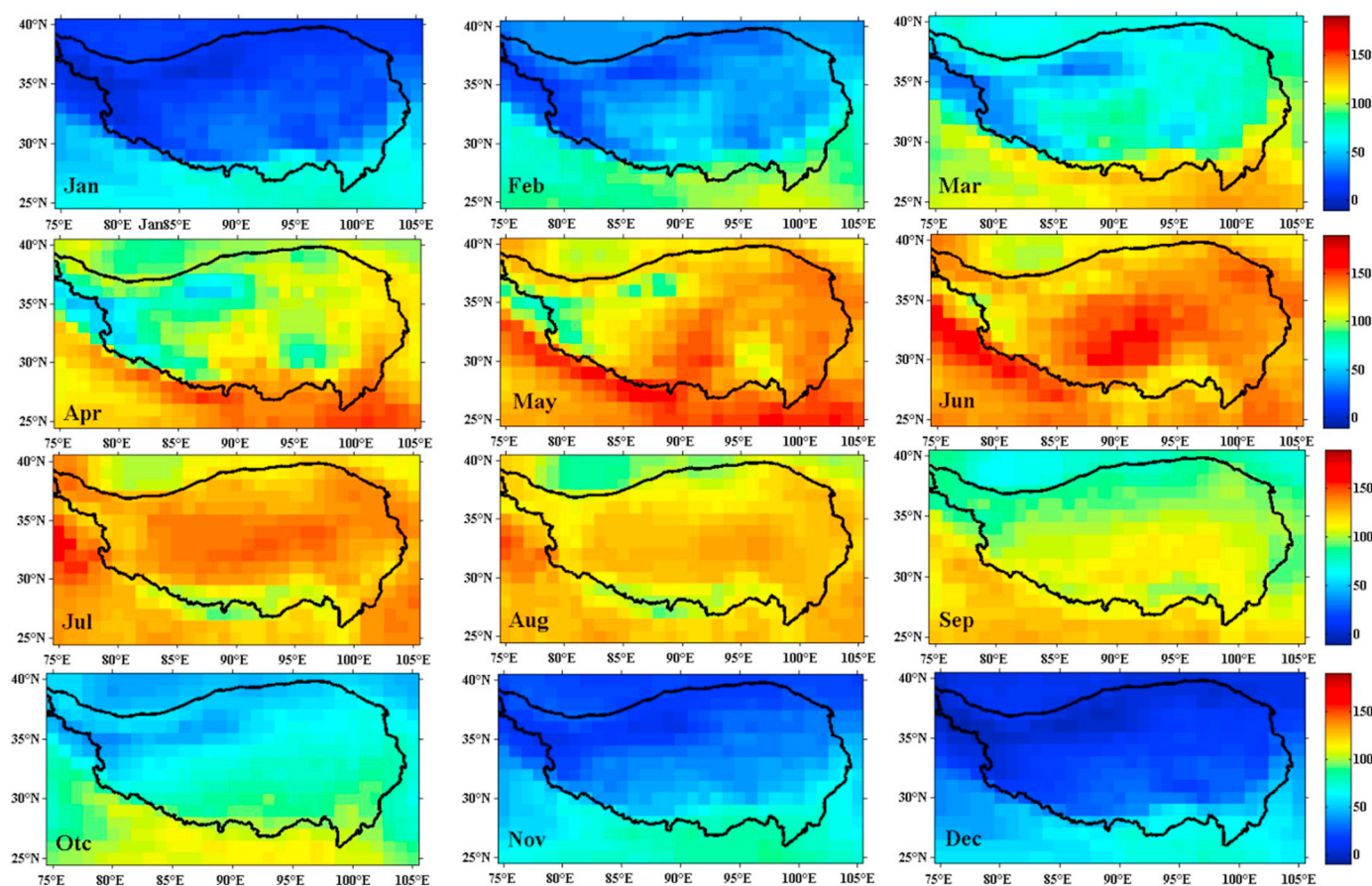


Fig. 8. The same as Fig. 6, but for net radiation heat flux.

RLUS and RSUS. The top five CMIP5 models for RLDS and RSDS are CNRM_CM5, CSIRO-Mk3-6-0 and CMCC-CMS, ACCESS1-3 and CSIRO-Mk3-6-0, MIROC5 and HadGEM2-ES, and MPI-ESM-MR and ACCESS1-0. These five models used for heat flux will be defined as optimal models.

3.1.2. Comparing the average multimodel and the best multimodel ensemble

R_n and G_0 were calculated according to Eqs. (1)–(2). Two ensemble simulations of land surface heat fluxes were compared with the observations in the permafrost regions at the Tanggula site in 2005, one only used the five optimal models, and the other used all 17 models. The difference in the climatology of extreme indices between the optimal/all model ensembles and the observations are shown in Fig. 4. The results show that the simulation of LE using the average multimodel ensemble was similar to the best multimodel ensemble. The difference between the simulated and the observed LE values ranged from -20 – 20 W/m^2 , with the majority ($> 40\%$) of difference values concentrated near 0 W/m^2 (Fig. 4). The results from the H_s simulations indicate that the simulation accuracy using the best multimodel ensemble was higher than that using the average multimodel ensemble (-20 – 20 W/m^2), with the majority ($> 25\%$) of difference values concentrated near 0 W/m^2 . Nonetheless, the simulations of R_n and G_0 using the average multimodel ensemble were better than those using the best multimodel ensemble, with the majority ($> 30\%$) of difference values concentrated near 0 W/m^2 (Fig. 4); in particular, G_0 generally ranged from -20 – 20 W/m^2 , which was far smaller than the difference range for the simulation result using the best multimodel ensemble.

The land surface heat flux results using the average multimodel ensemble were compared with observations in permafrost regions at

Tanggula site in 2005. The results show that the R values were 0.71, 0.48, 0.71 and 0.80, and the RMSEs were 24.07, 20.00, 41.09 and 7.86 W/m^2 for LE, H_s , R_n and G_0 , respectively. The results could follow the pattern of observed land surface heat fluxes (Fig. 5). Therefore, the results of the average multimodel ensemble were then performed.

3.2. Characteristics of the spatial distribution of land surface heat flux values

3.2.1. Spatial distribution of land surface heat flux values

As seen from Fig. 6, the average multimodel ensemble results show that the monthly average LE in 2005 was small in December and January, with a minimum value of 6.57 W/m^2 in January on the QTP. In March, the LE gradually increased along the southern edge of the QTP, reaching large values in June, July and August, which is when the rainy season occurs. In September, the LE gradually decreased. Looking at the characteristics of the whole distribution, it can be seen that a low-value center is located over the northwest QTP at high altitudes in the permafrost regions. Meanwhile, a high-value center is located over the southeastern region of the Malayalam Mountains, where it is clearly visible over the Qaidam basin.

Fig. 7 shows the average multimodel ensemble results for the monthly average H_s in 2005 on the QTP. It can be seen that H_s was negative in January and December northwest of the QTP, with a minimum value of -12.25 W/m^2 in December. In March, it gradually increased over the northeast QTP and reached large values in May and June, which gradually decreased in August. Looking at the characteristics of the overall distribution, a low-value center was located over high-altitude areas and along the southeast edge of the QTP, and a high-

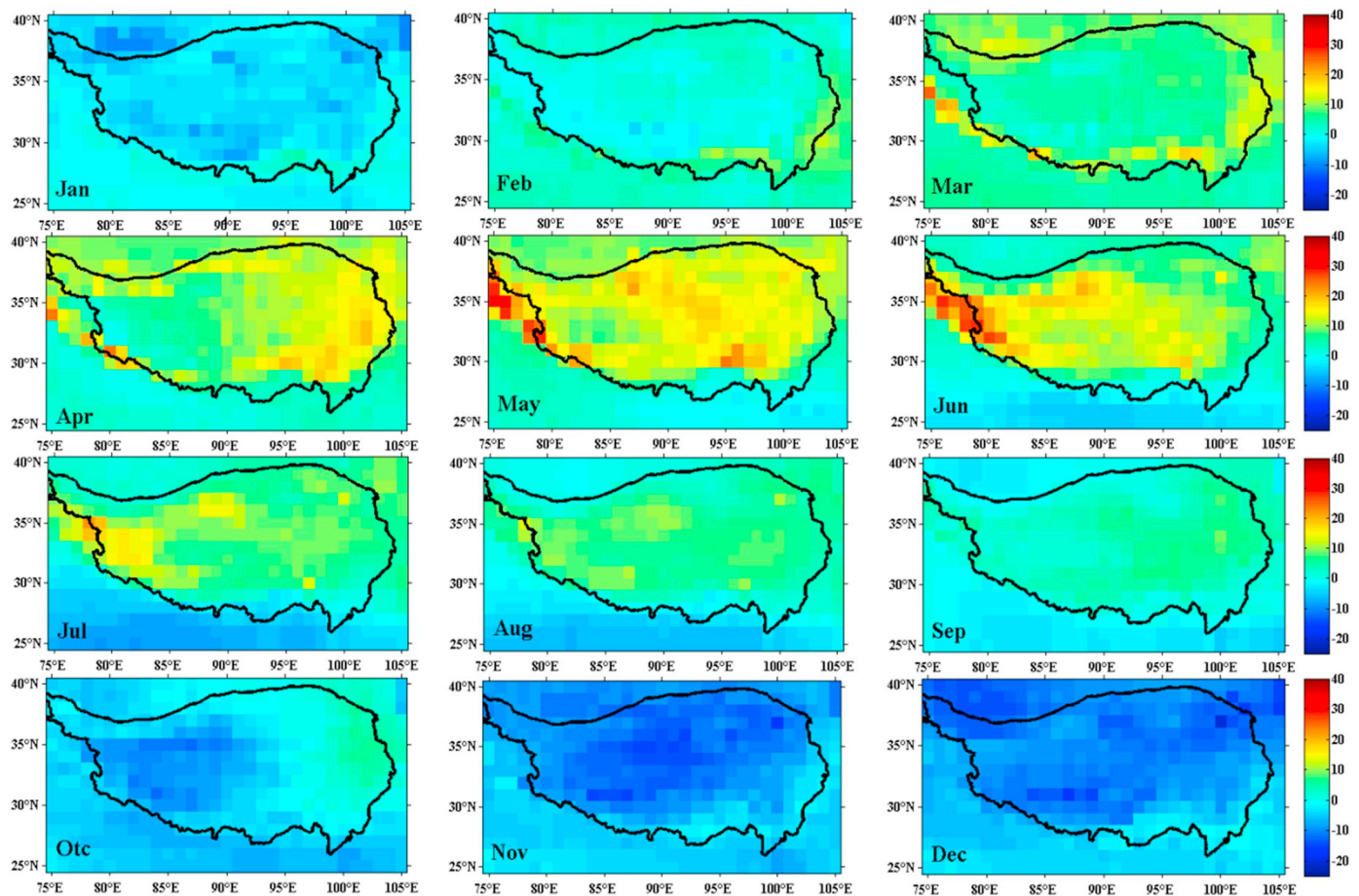


Fig. 9. The same as Fig. 6, but for soil heat flux.

value center was located over the northeast and southwest edges of the QTP. H_s was positive from March to October in most areas of the QTP.

For the monthly average R_n in 2005 (Fig. 8), it can be seen that it was smaller in December and January, with a minimum of -6.27 W/m^2 in January along the northwest edge of the QTP. In March, the monthly average net radiation began to increase gradually along the southeastern QTP, and it reached large values in May, June and July, with a maximum of 165.61 W/m^2 in June. Then, it gradually decreased in the beginning of August. In general, it was larger over the central QTP and smaller over the northwestern QTP.

The fluctuation in G_0 in 2005 was well correlated with R_n (Fig. 9). The positive and negative changes in G_0 were basically consistent with the identical soil freezing and thawing process in the active layer of the permafrost regions. Smaller values were detected in November and December, with a minimum of -20.47 W/m^2 . In March, it began to increase gradually over the southeastern QTP, and it reached large values in May, June and July, with a maximum of 32.42 W/m^2 in June. G_0 gradually decreased at the beginning of August. In general, it was larger over the central QTP and smaller over the northwestern QTP.

3.2.2. Spatial distribution of the Bowen ratio

The Bowen ratio was defined as the ratio of H_s to LE (Sverdrup, 1943). Fig. 10 show the variations in the monthly average distribution maps for the QTP in 2005; the Bowen ratio was stable between -0.81 and 4.86 , and the average ratio from March to June was greater than those in other months. The monthly average Bowen ratios in the permafrost regions were < 1.0 from July to September, and nearly all of the ratios exceeded 1.0 from January to April, which was when the soil

unfrozen water content was low, and the vegetation coverage was sparse; this resulted in the conversion of R_n primarily into H_s . In December and January, the monthly average Bowen ratio became negative. It can be seen that the Bowen ratio was larger in the central and northeastern QTP and smaller along the northwestern edge of the QTP (Fig. 10).

3.2.3. Spatial distribution of surface heating field intensity

For the monthly average surface heating field intensity in 2005 (Fig. 11), it can be seen that it was smaller in December, January and February, with a minimum of 2.43 W/m^2 in January in the northwestern QTP. In March, the monthly average surface heating field intensity began to increase gradually over the southeastern QTP, and it reached larger values in May, June and July, with a maximum of 164.22 W/m^2 in June. The amplitude of the surface heating field intensity was 161.79 W/m^2 . Then, it gradually reduced in the beginning of September. In general, it was larger over the central QTP and smaller over the northwestern QTP. The surface heat source intensity was positive over the QTP (Fig. 11).

4. Discussions

4.1. Variations in land surface heat fluxes over the QTP

The results presented in this study revealed that variations in monthly average land surface heat fluxes had larger differences due to factors such as a vast area, unique geographic setting and higher elevation (Li et al., 2006; Xiao et al., 2011). The main factors for seasonal

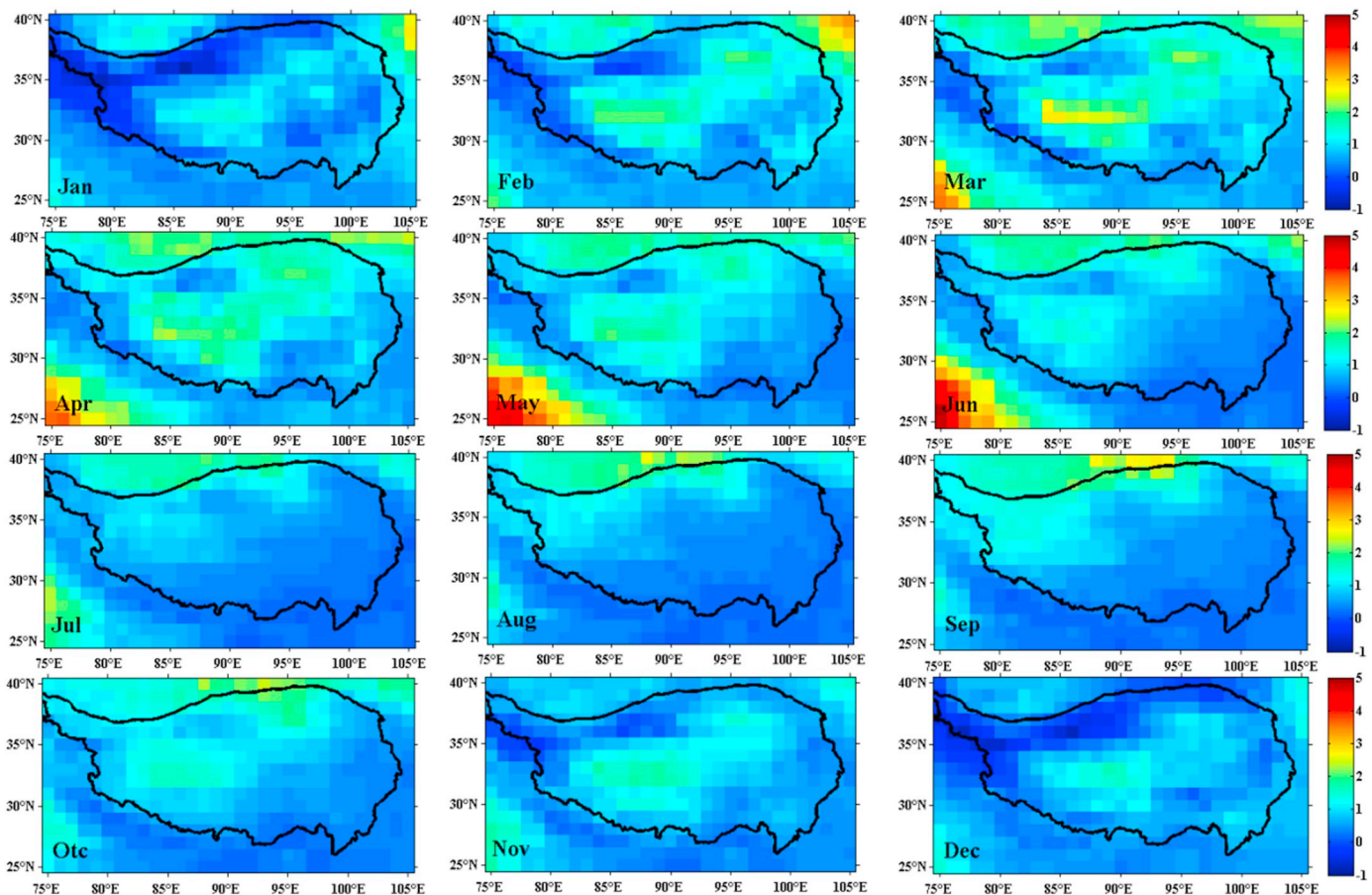


Fig. 10. The same as Fig. 6, but for Bowen ratio.

alternating characteristics of turbulent fluxes over the QTP are the Asian monsoon and the freezing-thawing processes of the active layer (Yao et al., 2011). From March to May, the H_s rapidly increased over the QTP. This was because solar radiation increased, which caused air temperatures to increase, and snow and ice began to melt, which caused the albedo to decrease (Wang et al., 2013; Xiao et al., 2011). At the same time, LE also increased gradually due to precipitation, which mainly derived from surface evapotranspiration processes and soil moisture (Wang and Shang, 2007). It can be seen that LE is the strongest over the southeastern QTP from May to August, especially in July (Fig. 6), which had a value greater than that for H_s . This important result is because the monsoon usually occurs from May to October over the QTP (Parthasarathy et al., 1992; Wang and Fan, 1999); precipitation was concentrated from June to September, which led to a significant increase in the surface soil moisture content (Yao et al., 2008; Yao et al., 2011). Meanwhile, precipitation decreased over the northwest QTP, which could be because evapotranspiration decreased from the southeast to northwest over the QTP (Peng et al., 2016). In contrast, H_s was the weakest over the southeast QTP, and it gradually increased, which contributed to the northwest QTP (Fig. 7). In September, LE and H_s decreased with a decrease in solar radiation and surface ground temperature. LE was strongest in November, December, January and February over the southeastern QTP, and H_s was the primary constituent in other areas (Ji and Huang, 2006). However, the LE and H_s in the northeastern QTP were almost equivalent, whereas previous studies showed that H_s mainly occurred in winter, while LE occurred in spring, summer and autumn over the northern QTP (Xiao et al., 2011); this was because the simulated precipitation in the CMIP5 models was larger over the QTP (Li et al., 2013).

Net radiation was the largest from June to July and smallest in January and December (Fig. 8), which was mainly influenced by the solar altitude angle, clouds and reflectivity (Li et al., 2007; Xiao et al., 2011). The variation trend for surface heating field intensity was the same as that of R_n because it was mainly affected by R_n , and the G_0 was much smaller compared to the R_n (Li et al., 2007). The results also revealed that there was a good correlation between the surface heating field intensity (E_s) and R_n , with a correlation coefficient was 0.99. The regression equation was $E_s = 1.08R_n - 5.49$. The results were in close agreement with those at the Wudaoliang site regarding permafrost regions on the QTP (Li et al., 2007). The surface heating field intensity was positive over the QTP (Fig. 11), which indicated that the Plateau was a heat source (Chen et al., 2014a), and had different regional patterns; the eastern QTP exhibited stronger heating than the western QTP, and the southern QTP exhibited greater heating than the northern QTP (Yang et al., 2011a). Meanwhile, the hinterland of the QTP had greater heating than the surrounding areas of the QTP. This was mainly because the eastern and southern QTP was characterized as a monsoon region with strong wind speeds (Wang and Fan, 1999). The western QTP perennial snow distribution and the ground albedo were large, and the shortwave radiation absorbed by the ground was reduced. The northern QTP was majorly characterized by bare ground; evaporation and thermal roughness were very small, and the differences between air and ground temperatures were larger (Wang et al., 2013).

4.2. Impacts of the freezing and thawing process on land surface heat fluxes in permafrost regions

The freeze-thaw process of soil is exceedingly complex, as it

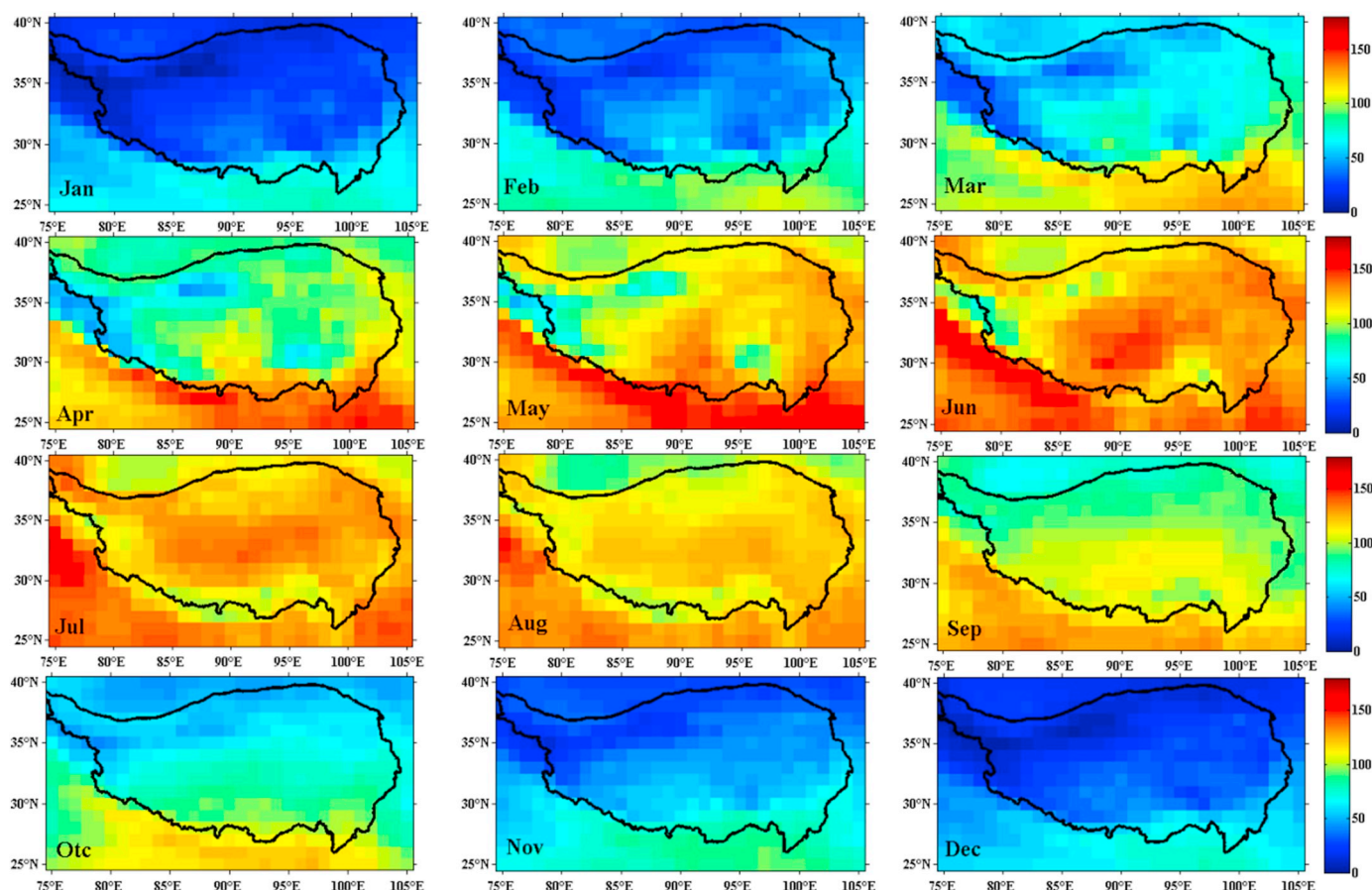


Fig. 11. The same as Fig. 6, but for surface heating field intensity.

involves a variety of physical and chemical changes, including energy transfers, phase changes, and salt accumulation (Chen et al., 2014a; Hu et al., 2015). In general, the summer thawing stage occurred from April to September in the northern QTP (Zhao et al., 2000), and there were obvious variation characteristics for R_n , G_0 and the surface heat source intensity, which were strongest in May, June and July (Figs. 8, 9 and 11, respectively). The monthly average of G_0 was positive from April to September, indicating that the soil absorbed energy from the atmosphere, the soil temperatures in the active layer decreased from the ground surface downwards, and the active layer was absorbing heat from the atmosphere and transferring it downwards (Zhao et al., 2000). Meanwhile, the land surface heat fluxes were lowest, and the monthly average soil heat flux was negative in November, December and January during the freeze stage, indicating that energy was generally transferred from the soil to the atmosphere (Chen et al., 2014a). Because there were no phase change processes, LE and H_s were smaller than those in other months. The seasonal variation process was the same as the soil freezing and thawing process in permafrost regions, indicating that soil began to thaw between April and May as the cold season transitioned into a warm season. In September and October, the surface energy collapsed, and the warm season turned into a cold season when the soil began to freeze (Li et al., 2011).

The Bowen ratio is the quotient of H_s and LE , which reflects the distribution of energy and is closely related to the seasonal variations in turbulent fluxes due to the monsoon and the freezing and thawing processes of the soil at BJ and Tanggula sites on the QTP (Gu et al., 2015). The Bowen ratio at the beginning of the soil freezing (October) and thawing (April and May) stages is greater than that during the final thawing stage (Fig. 10). Guo et al. (2011) found that the Bowen ratio

was higher during the freezing and thawing stages than that in the completely thawed stage, which indicates that unfrozen water content present during diurnal freeze-thaw cycles has a significant impact on latent heat flux, and the frequent occurrence of surface freeze-thaw cycles affect the distribution of energy (Chen et al., 2014a). The Bowen ratio is < 1.0 between June and September in most areas of the QTP, which indicates that the monthly average LE is greater than H_s , as precipitation increases the soil water content, which increases the evaporation (Ge et al., 2016; Zhang et al., 2016). On the other hand, the soil and air temperature difference is relatively small because the sensible heat flux was small (Li et al., 2007). There is a great variation difference in the spatial variation of the freeze stage (January–March, November and December), which is > 1.0 . This result is in agreement with Yao et al. (2008) and Xiao et al. (2011), whose studies were based on observational station data at the Tanggula site in the permafrost region; the Bowen ratios were 0.7 and 0.79 on average in summer and autumn and 3.4 and 1.56 on average in winter and spring, respectively. It should be noted that the monthly average Bowen ratios range from -0.81 to 4.86 , which is higher than that in other ecosystems, such as arid and semiarid areas, grasslands and arctic tundras (Eugster et al., 2000; Kalthoff et al., 2006). The average annual Bowen ratio is approximately 1.0, which is lower than the average annual results from Li et al. (2007) in 1994 and 2000 at the Wudaoliang site (4.0) and those from Zhang et al. (2016) at the Beiluhe site in the permafrost region of the QTP (3.82).

4.3. Model uncertainties and reasons for discrepancies

Previous studies have shown that the Bowen ratio ranged from 2.96

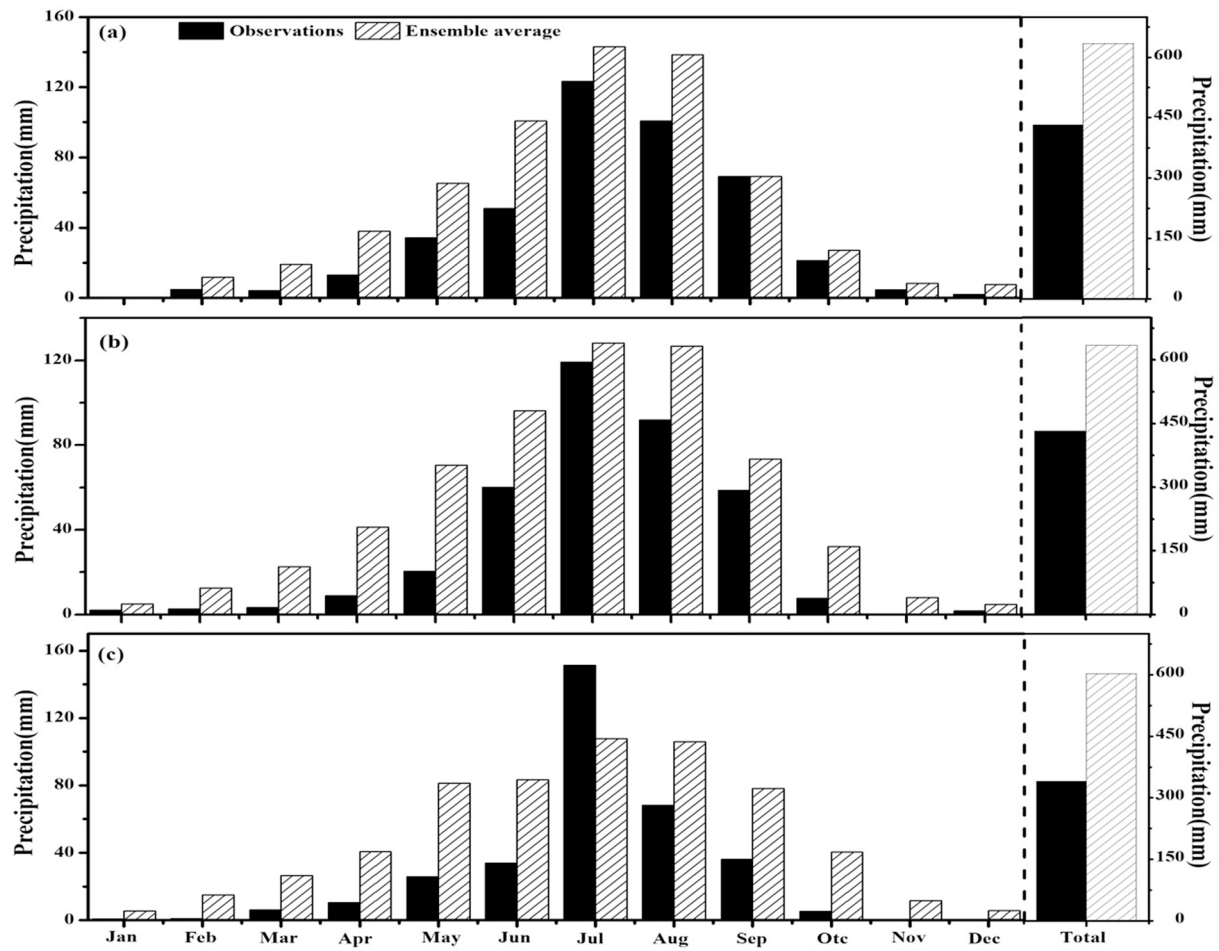


Fig. 12. The monthly average precipitation simulated by the average multi-model ensemble vs. observed: (a): Tanggula; (b): Tuotuohe; (c): Wudaoliang in 2005.

Table 2

RE (relative error) of the monthly average air temperature simulated by the average multi-model ensemble and observations at Tanggula, Tuotuohe and Wudaoliang in 2005.

Month	Tanggula			Tuotuohe			Wudaoliang		
	Obs	Ens	RE (%)	Obs	Ens	RE (%)	Obs	Ens	RE (%)
Jan	-14.87	-19.00	-27.79	-13.85	-19.43	-40.23	-14.72	-18.16	-23.36
Feb	-13.84	-16.49	-19.14	-11.78	-16.89	-43.41	-13.19	-15.47	-17.27
Mar	-8.46	-11.81	-39.70	-6.56	-12.83	-95.47	-9.00	-11.50	-27.81
Apr	-5.74	-5.14	-10.37	-3.44	-6.33	-84.10	-5.44	-4.90	-10.05
May	-1.98	0.41	-120.72	1.16	-0.66	157.19	-0.95	0.42	-143.58
Jun	3.03	4.80	58.34	5.46	3.81	30.32	3.45	4.54	31.61
Jul	5.10	6.11	19.90	8.21	5.31	35.35	5.97	6.16	3.15
Aug	5.60	5.34	4.57	8.42	4.60	45.38	6.29	5.33	15.33
Sep	2.96	2.28	22.84	5.01	1.32	73.67	3.01	1.71	43.36
Oct	-5.12	-4.63	-9.66	-2.14	-5.53	-158.85	-4.23	-4.92	-16.14
Nov	-12.22	-12.74	-4.25	-9.97	-13.56	-36.10	-11.19	-12.19	-8.86
Dec	-13.69	-18.06	-31.90	-14.60	-18.85	-29.11	-14.89	-17.32	-16.29

to 5.64 over a whole year, and H_s was greater than LE in November and December and from January to April in the permafrost region of the QTP (Xiao et al., 2011; You et al., 2017; Zhou and Du, 2016). However, the monthly average Bowen ratios were lower in our study. One reason may be because the monthly average precipitation simulated by the average multimodel ensemble was greater than that observed in 2005. It can be seen that the simulated monthly average and annual precipitation was almost more than those from the observations at the

Tanggula, Tuotuohe and Wudaoliang sites in the permafrost region of the QTP; the simulated annual precipitation using the average multi-model ensemble was 634.55 mm, 621.45 mm and 602.39 mm, and the observation values were 432.41 mm, 376.90 mm and 340 mm, respectively (Fig. 12). At low latitudes in the northwest arid region of China, the simulated annual precipitation using the CMIP5 was generally greater than that of the observed, which ranged from 200 to 300 mm over the QTP, especially in spring and winter (Chen et al., 2014b; Hu

Table 3

RE (relative error) of the monthly average surface temperature simulated by the average multi-model ensemble and observations at Tanggula, Tuotuohe and Wudaoliang in 2005.

Month	Tanggula			Tuotuohe			Wudaoliang		
	Obs	Ens	RE (%)	Obs	Ens	RE (%)	Obs	Ens	RE (%)
Jan	−11.72	−19.18	−63.61	−13.45	−19.33	−43.68	−12.30	−18.26	−48.48
Feb	−10.66	−16.15	−51.42	−10.70	−16.23	−51.73	−9.87	−14.92	−51.20
Mar	−5.12	−10.71	−109.05	−2.32	−11.77	−407.65	−3.52	−10.80	−206.86
Apr	−2.32	−3.32	−42.98	1.90	−4.24	323.34	1.17	−3.05	360.09
May	1.55	2.70	73.72	8.02	1.78	77.78	5.41	2.70	50.04
Jun	6.71	6.90	2.75	12.39	6.32	48.99	10.63	6.75	36.51
Jul	8.84	8.02	9.27	13.59	7.50	44.82	9.81	8.35	14.87
Aug	9.36	6.88	26.48	13.97	6.36	54.52	9.71	7.11	26.78
Sep	6.64	3.65	45.06	9.44	2.87	69.58	7.08	3.46	51.12
Oct	−1.68	−3.42	−103.33	1.60	−4.68	392.25	0.41	−3.93	1052.05
Nov	−8.99	−11.80	−31.19	−8.79	−13.36	−51.95	−7.72	−11.97	−55.18
Dec	−10.51	−18.10	−72.25	−13.99	−19.06	−36.26	−12.70	−17.45	−37.37

Table 4

RE (relative error) of the difference between the monthly average surface temperature and air temperature simulated by the average multi-model ensemble and observations at Tanggula, Tuotuohe and Wudaoliang in 2005.

Month	Tanggula			Tuotuohe			Wudaoliang		
	Obs	Ens	RE (%)	Obs	Ens	RE (%)	Obs	Ens	RE (%)
Jan	3.15	−0.18	105.71	0.40	0.10	74.97	2.43	−0.10	103.97
Feb	3.18	0.34	89.17	1.08	0.66	39.03	3.32	0.55	83.42
Mar	3.34	1.11	66.79	4.25	1.06	75.09	5.48	0.70	87.23
Apr	3.41	1.82	46.61	5.34	2.10	60.71	6.62	1.84	72.13
May	3.53	2.29	35.32	6.86	2.44	64.39	6.37	2.29	64.07
Jun	3.68	2.10	43.06	6.93	2.51	63.71	7.18	2.21	69.19
Jul	3.74	1.91	49.00	5.38	2.19	59.25	3.84	2.19	42.91
Aug	3.76	1.54	59.07	5.55	1.76	68.37	3.41	1.78	47.89
Sep	3.68	1.37	62.88	4.43	1.55	64.96	4.06	1.75	56.87
Oct	3.44	1.21	64.90	3.74	0.85	77.20	4.65	0.98	78.81
Nov	3.23	0.94	70.88	1.17	0.20	82.67	3.48	0.21	93.93
Dec	3.18	−0.04	101.29	0.61	−0.22	135.86	2.19	−0.13	106.16

et al., 2014; Li et al., 2013; Wu et al., 2017). The LE was mainly constrained by precipitation and surface soil moisture, which increased significantly in winter and spring when precipitation occurred (Sun et al., 2014). The overestimation of precipitation by the CMIP5 models also caused an increase in LE (Han et al., 2017; Yang et al., 2014).

In addition, the wind speed and ground air temperature gradients combined determined H_s . Generally, the greater the wind speed and the difference between ground and air temperatures, the greater the sensible heat flux (Yang et al., 2011b). The results revealed that the monthly average air and surface temperatures simulated by the average multimodel ensemble were lower than those from the observations at the Tanggula, Tuotuohe and Wudaoliang sites in 2005, excluding the air temperature at the Tanggula and Wudaoliang sites from May to July (Tables 2 and 3). Previous studies indicated that the CMIP5 models underestimated the mean annual surface air temperature (−2.3 °C), and the negative deviation was relatively large in autumn and winter over the QTP (Hu et al., 2014; Wu et al., 2017), which was consistent with the results from this study. Meanwhile, the difference in the simulated monthly average surface temperature and the air temperature was much lower than that from the observations at the Tanggula, Tuotuohe and Wudaoliang sites, which had relative errors from 35.32% to 135.86% (Table 4). In addition, the simulated monthly average 10 m wind speed was lower than that of the observations at the Tanggula and Wudaoliang sites in 2005 (Fig. 13). This could be because the H_s were underestimated by the average multimodel ensemble in the permafrost regions of the QTP, which attributed to a decrease in both the wind speed and the difference between ground and air temperatures.

Other possible reasons for the discrepancies in land surface fluxes was that the complexities and differences among the land surface, radiation, and boundary layer parameterization schemes contributed to large differences in land surface fluxes in permafrost regions over the QTP (Zhou and Du, 2016); these complexities and differences could be caused by imperfect pattern dynamics and physical processes, low resolution and a poor description of terrain features in the permafrost regions (Hu et al., 2014; Su et al., 2013). Additionally, cloudiness plays an important role in surface sensible heat flux due to its influence on shortwave and longwave net fluxes, as well as its impact on soil temperature (Zhou and Du, 2016). It is necessary to further improve the model, especially when coupling the physical processes that are suitable for permafrost on the QTP.

5. Conclusions

This study evaluated the performances of seventeen selected CMIP5 GCMs at the Tanggula site in the permafrost region of the QTP. It is revealed by the evaluation result in this study that these GCM simulations do not perform well for H_s , RSDS and RSUS, with correlation coefficients lower than 0.50. After comparing the average multimodel ensemble with the best multimodel ensemble, the results showed that the average multimodel ensemble was closer to the observed land surface heat fluxes. The average multimodel ensemble results showed that the monthly average values of LE and R_n in 2005 were small in December and January and large in May, June and July. The fluctuation in the soil heat flux was well correlated with R_n , and H_s were

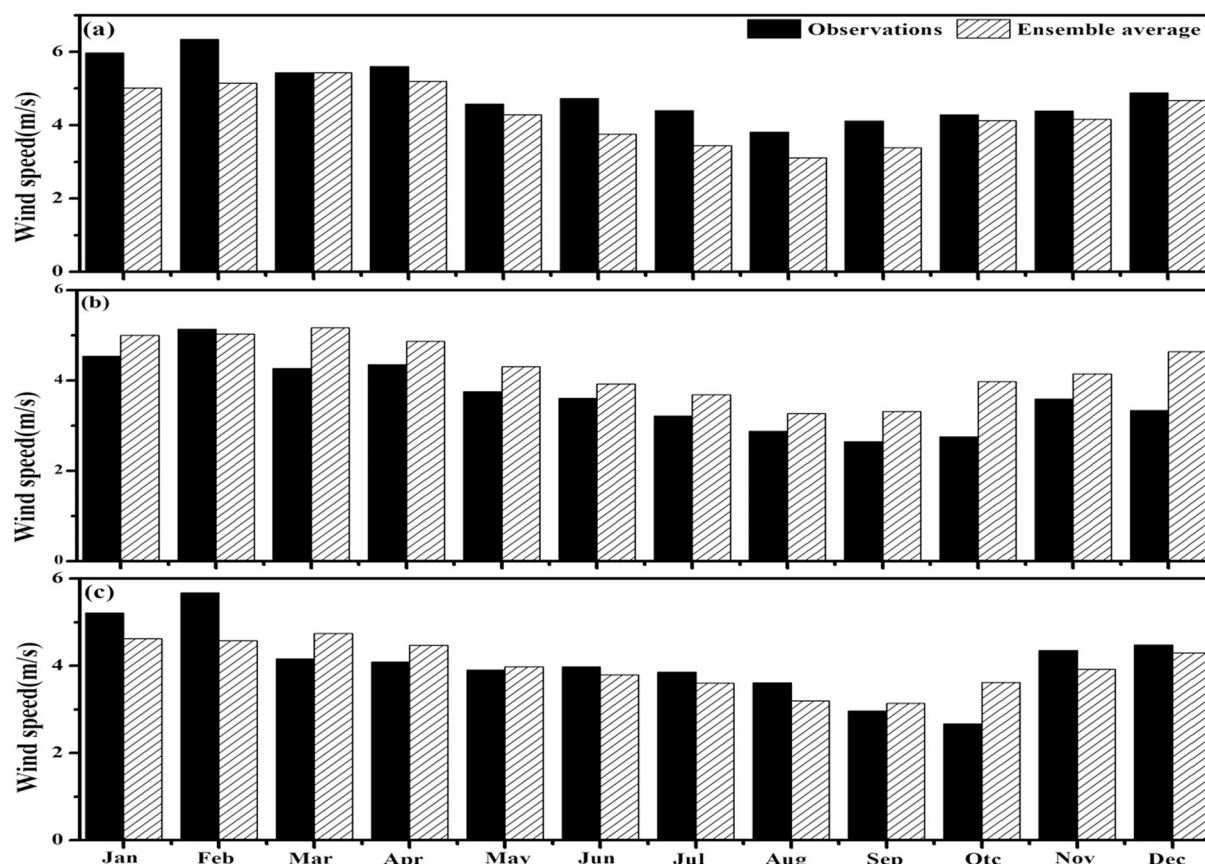


Fig. 13. The monthly average wind speed (10 m) simulated by the multi-model ensemble vs. observed: (a): Tanggula; (b): Tuotuohe; (c): Wudaoliang in 2005.

negative in January and December northwest of the QTP. R_n and G_0 were large over the central QTP and small over the northwest QTP. The Bowen ratio was large over the central and northeastern QTP and small along the northwestern edge of the QTP. The results also revealed that there was a good correlation between the surface heating field intensity and R_n , with a correlation coefficient of 0.99. The surface heating field intensity was positive over the QTP, which indicated that the Plateau was a heat source. Soil freezing and thawing processes in permafrost regions have substantial influence on seasonal variations in the land surface heat flux. The Bowen ratio was higher during the freezing and thawing stages than in the completely thawed stage, and it was < 1.0 between June and September in most areas of the QTP. However, it was found that differences existed in terms of the spatial and temporal patterns of land surface heat flux due to the overestimation of precipitation, smaller differences between the simulated monthly average surface temperature and the observed air temperature, and lower wind speeds when using the CMIP5 models in permafrost region on the QTP. Further research is required to investigate and improve the physical processes in the GCMs related to permafrost on the QTP.

Acknowledgements

This work was financially supported by the National Natural Science Foundation of China (41601078), the Strategic Priority Research Program of Chinese Academy of Sciences (XDA20020102), the Science Fund for Creative Research Groups of National Natural Science Foundation of China (41721091), the National Natural Science Foundation of China (41871060, 41690142, 41671070, 41771076), and the Excellent Youth Scholars of Northwest Institute of Eco-Environment and Resources, Chinese Academy of Sciences.

References

- Chang, Y., Lü, S., Luo, S., Wu, J., Li, S., 2016. Evaluation and Projections of Permafrost on the Qinghai-Xizang Plateau by CMIP5 Coupled Climate Models. *Plat. Meteorol.* 35, 1157–1168.
- Chen, B., Luo, S., Lu, S., Zhang, Y., Ma, D., 2014a. Effects of the soil freeze-thaw process on the regional climate of the Qinghai-Tibet Plateau. *Clim. Res.* 59, 243–257.
- Chen, X., Xu, Y., Xu, C., Yao, Y., 2014b. Assessment of precipitation simulations in China by CMIP5 multi-models. *Progressus Inquisitiones de Mutatione Climatis* 10, 217–225.
- Cheng, G., 1990. Recent development of geocryological study in China. *Acta Geograph. Sin.* 45, 220–223.
- Eugster, W., Rouse, W., Pielke, R., McFadden, J., Baldocchi, D., Kittel, T., Chapin, F., Liston, G., Vidale, P., Vaganov, E., Chambers, S., 2000. Land-atmosphere energy exchange in Arctic tundra and boreal forest: available data and feedbacks to climate. *Glob. Chang. Biol.* 6, 84–115.
- Ge, J., Yu, Y., Li, Z., Xie, J., Liu, C., Zan, B., 2016. Impacts of freeze/thaw processes on land surface energy fluxes in the permafrost region of Qinghai-Xizang Plateau. *Plat. Meteorol.* 35, 608–620.
- Gu, L., Yao, J., Hu, Z., Zhao, L., 2015. Comparison of the surface energy budget between regions of seasonally frozen ground and permafrost on the Tibetan Plateau. *Atmos. Res.* 153, 553–564.
- Guo, D., Yang, M., Li, M., Qu, P., 2009. Analysis on simulation of characteristic of land surface energy flux in seasonal frozen soil region of Central Tibetan Plateau. *Plat. Meteorol.* 28, 978–987.
- Guo, C., Yang, M., Wang, H., 2011. Characteristics of land surface heat and water exchange under different soil freeze/thaw conditions over the central Tibetan Plateau. *Hydrol. Process.* 25, 2531–2541.
- Han, C., Ma, Y., Chen, X., Su, Z., 2017. Trends of land surface heat fluxes on the Tibetan Plateau from 2001 to 2012. *Int. J. Climatol.* 37, 4757–4767.
- Hu, Q., Jiang, D., Fan, G., 2014. Evaluation of CMIP5 models over the Qinghai-Tibetan Plateau. *Chin. J. Atmos. Sci.* 38, 924–938.
- Hu, G., Zhao, L., Li, R., Li, R., Wu, X., Wu, T., Xie, C., Zhu, X., Su, Y., 2019. Variations in soil temperature from 1980 to 2015 in permafrost regions on the Qinghai-Tibetan Plateau based on observed and reanalysis products. *Geoderma* 337, 893–905.
- Hu, G., Zhao, L., Wu, X., Li, R., Wu, T., Xie, C., Pang, Q., Xiao, Y., Li, W., Qiao, Y., Shi, J., 2015. Modeling permafrost properties in the Qinghai-Xizang (Tibet) Plateau. *Sci. China Earth Sci.* 58, 2309–2326.
- Hu, G., Zhao, L., Wu, X., Li, R., Wu, T., Xie, C., Qiao, Y., Li, W., Cheng, G., 2016. New

- Fourier-series-based analytical solution to the conduction-convection equation to calculate soil temperature, determine soil thermal properties, or estimate water flux. *Int. J. Heat Mass Transf.* 95, 815–823.
- Ji, J., Huang, M., 2006. The estimation of the surface energy fluxes over Tibetan Plateau. *Adv. Earth Science* 21, 1268–1272.
- Jiang, S., Jiang, Z., Li, W., Shen, Y., 2017. Evaluation of the extreme temperature and its trend in China simulated by CMIP5 models. *Progressus Inquisitiones de Mutatione Climatis* 13, 11–24.
- Kalthoff, N., Fiebigwittmaack, M., Meissner, C., Kohler, M., Uriarte, M., Bischoffgauss, I., Gonzales, E., 2006. The energy balance, evapo-transpiration and nocturnal dew deposition of an arid valley in the Andes. *J. Arid Environ.* 65, 420–443.
- Kang, S., Xu Y., You, Q., Fluegel, W., Pepin, N., Yao, T., 2010. Review of climate and cryospheric change in the Tibetan Plateau. *Environ. Res. Lett.* 5, 1–8.
- Li, M., Ma, Y., Ma, W., Hu, Z., Ishikawa, H., Su, Zh., Sun, F., 2006. Analysis of turbulence characteristics over the northern Tibetan Plateau area. *Adv. Atmos. Sci.* 23, 579–585.
- Li, R., Zhao, L., Ding, Y., Yang, W., Hu, Z., Ji, G., 2007. The features of each components in the surface heat balance equation over Wudaoliang northern Tibetan Plateau. *J. Mt. Sci.* 25, 664–670.
- Li, R., Zhao, L., Ding, Y., Wang, Y., Du, E., Liu, G., Xiao, Y., Sun, L., Liu, Y., Shi, W., 2011. Impact of surface energy variation on thawing processes within active layer of permafrost. *J. Glaciol. Geocryol.* 33, 1235–1242.
- Li, R., Zhao, L., Ding, Y., Wu, T., Xiao, Y., Du, E., Liu, G., Qiao, Y., 2012. Temporal and spatial variations of the active layer along the Qinghai-Tibet Highway in a permafrost region. *Chin. Sci. Bull.* 57, 4609–4616.
- Li, Z., Wei, Z., Lu, S., Gao, Y., Han, B., Li, S., Ao, Y., Chen, H., 2013. Verifications of surface air temperature and precipitation from CMIP5 model in northern Hemisphere and Qinghai-Xizang Plateau. *Plat. Meteorol.* 32, 921–928.
- Liu, X., Chen, B., 2000. Climatic warming in the Tibetan Plateau during recent decades. *Int. J. Climatol.* 20, 1729–1742.
- Ma, W., Ma, Y., 2016. Modeling the influence of land surface flux on the regional climate of the Tibetan Plateau. *Theor. Appl. Climatol.* 125, 45–52.
- Ma, W., Ma, Y., Li, M., Su, B., Wang, J., 2005. Seasonal variation on land surface energy budget and energy balance components in the northern Tibetan Plateau. *J. Glaciol. Geocryol.* 27, 673–679.
- Ma, Y., Su, Z., Li, Z., Koike, T., Menenti, M., 2006. Determination of regional distributions and seasonal variations of land surface heat fluxes from Landsat-7 Enhanced Thematic Mapper data over the central Tibetan Plateau area. *J. Geophys. Res. Atmos.* 111, 2963–2971.
- Ma, W., Ma, Y., Su, B., 2011. Feasibility of retrieving land surface heat fluxes from ASTER data using SEBS: a case study from the NamCo Area of the Tibetan Plateau. *Arct. Antarct. Alp. Res.* 43, 239–245.
- Parthasarathy, B., Kumar, K.R., Kothawale, D.R., 1992. Indian-summer monsoon rainfall indexes-1871–1990. *Meteorol. Mag.* 121, 174–186.
- Peng, J., Loew, A., Chen, X., Ma, Y., Su, Z., 2016. Comparison of satellite-based evapo-transpiration estimates over the Tibetan Plateau. *Hydrol. Earth Syst. Sci.* 20, 3167–3182.
- Qiu, J., 2008. The third pole. *Nature* 454, 393–396.
- Su, F., Duan, X., Chen, D., Hao, Z., Cuo, L., 2013. Evaluation of the global climate models in the CMIP5 over the Tibetan Plateau. *J. Clim.* 26, 3187–3208.
- Sun, L., Zhao, L., Li, Ren, Yao, J., Liu, Y., Qiao, Y., Jiao, K., 2014. Effects of precipitation on the permafrost ground surface energy fluxes. *J. Longdong Univ.* 01, 41–46.
- Sverdrup, H., 1943. On the ratio between heat conduction from the sea surface and heat used for evaporation. *Ann. NY Acad. Sci.* 44, 81–88.
- Tang, M., Sheng, Z., Chen, Y., 1979. On climatic characteristics of the Xizang Plateau monsoon. *Acta Geograph. Sin.* 34, 34–42.
- Taylor, K.E., Stouffer, R.J., Meehl, G.A., 2012. An overview of cmip5 and the experiment design. *Bull. Am. Meteorol. Soc.* 93, 485–498.
- Wang, B., Fan, Z., 1999. Choice of south Asian summer monsoon indices. *Bull. Am. Meteorol. Soc.* 80, 629–638.
- Wang, C., Shang, D., 2007. Effect of the variation of the soil temperature and moisture in the transition from dry-season to wet-season over northern Tibet Plateau. *Plat. Meteorol.* 26, 677–685.
- Wang, C., Shi, R., 2007. Simulation of the land surface processes in the western Tibetan Plateau in summer. *J. Glaciol. Geocryol.* 29, 73–81.
- Wang, S., Xiong, Z., 2004. The preliminary analysis of 5 coupled ocean-atmosphere global climate models simulation of regional climate in Asia. *Clim. Environ. Res.* 9, 240–249.
- Wang, X., Yang, M., Wan, G., 2013. Temporal-spatial distribution and evolution of surface sensible heat flux over Qinghai-Xizang Plateau during last 60 years. *Plat. Meteorol.* 32, 1557–1567.
- Wu, J., Wang, B., Yang, Y., Chang, Y., Chen, L., Yang, J., Liu, X., 2017. Comparing simulated temperature and precipitation of CMIP3 and CMIP5 in arid areas of north-west China. *Progressus Inquisitiones de Mutatione Climatis* 13, 198–212.
- Xiao, Y., Zhao, L., Li, R., Yao, J., 2011. Seasonal variation characteristics of surface energy budget components in permafrost regions of northern Tibetan Plateau. *J. Glaciol. Geocryol.* 33, 1033–1039.
- Yanai, M., Wu, G.X., 2006. Eff. Tibetan Plat. 29. pp. 513–549.
- Yanai, M.H., Li, C.F., Song, Z.S., 1992. Seasonal heating of the Tibetan Plateau and its effects on the evolution of the Asian summer monsoon. *J. Meteorol. Soc. Jpn.* 70, 319–351.
- Yang, K., Koike, T., Yang, D.W., 2003. Surface flux parameterization in the Tibetan Plateau. *Bound.-Layer Meteorol.* 106, 245–262.
- Yang, K., Guo, X., He, J., Qin, J., Koike, T., 2011a. On the climatology and trend of the atmospheric heat source over the Tibetan Plateau: an experiments-supported revisit. *J. Clim.* 24, 1525–1541.
- Yang, K., Guo, X.F., Wu, B.Y., 2011b. Recent trends in surface sensible heat flux on the Tibetan Plateau. *Sci. China Earth Sci.* 54, 19–28.
- Yang, K., Wu, H., Qin, J., Lin, C., Tang, W., Chen, Y., 2014. Recent climate changes over the Tibetan Plateau and their impacts on energy and water cycle: a review. *Glob. Planet. Chang.* 112, 79–91.
- Yao, J., Zhao, L., Ding, Y., Gu, L., Jiao, K., Qiao, Y., Wang, Y., 2008. The surface energy budget and evapotranspiration in the Tanggula region on the Tibetan Plateau. *Cold Reg. Sci. Technol.* 52, 326–340.
- Yao, J., Zhao, L., Gu, L., Qiao, Y., Jiao, K., 2011. The surface energy budget in the permafrost region of the Tibetan Plateau. *Atmos. Res.* 102, 394–407.
- Ye, D., Gao, Y., 1979. The Meteorology of the Qinghai-Xizang (Tibet) Plateau. Science Press, Beijing (278 pp).
- Yin, Y., Wu, S., Zhao, D., 2013. Past and future spatiotemporal changes in evapo-transpiration and effective moisture on the Tibetan Plateau. *J. Geophys. Res.-Atmos.* 118, 10850–10860.
- You, Q., Min, J., Kang, S., 2016. Rapid warming in the Tibetan Plateau from observations and CMIP5 models in recent decades. *Int. J. Climatol.* 36, 2660–2670.
- You, Q., Xue, X., Peng, F., Dong, S., Gao, Y., 2017. Surface water and heat exchange comparison between alpine meadow and bare land in a permafrost region of the Tibetan Plateau. *Agric. For. Meteorol.* 232, 48–65.
- You, Q., Jiang, Z., Wang, D., Pepin, N., Kang, S., 2018. Simulation of temperature extremes in the Tibetan Plateau from CMIP5 models and comparison with gridded observations. *Clim. Dyn.* 51, 355–369.
- Zeng, Q., Zhang, X., Yuan, C., 1989. The concept, method and current studying situation of the climate models. *Adv. Earth Science* 3, 1–26.
- Zhang, M., Wen, Z., Xue, K., Chen, L., Li, D., Gao, Q., 2016. Surface energy budget analysis in permafrost region of Beiluhe area. *J. Arid Land Resour. Environ.* 30, 134–138.
- Zhao, L., Cheng, G.D., Li, S.X., Zhao, X.M., Wang, S.L., 2000. Thawing and freezing processes of active layer in Wudaoliang region of Tibetan Plateau. *Chin. Sci. Bull.* 45, 2181–2187.
- Zhao, L., Wu, Q., Marchenko, S.S., Sharkhuu, N., 2010. Thermal state of permafrost and active layer in central Asia during the international polar year. *Permafr. Periglac. Process.* 21, 198–207.
- Zhou, L., Du, Z., 2016. Regional differences in the surface energy budget over China: an evaluation of a selection of CMIP5 models. *Theor. Appl. Climatol.* 124, 241–266.
- Zhou, D., Huang, R., 2012. Response of water budget to recent climatic changes in the source region of the Yellow River. *Chin. Sci. Bull.* 57, 2155–2162.
- Zhou, X., Zhao, P., Chen, J., Chen, L., Li, W., 2009. Impacts of thermodynamic processes over the Tibetan Plateau on the northern Hemispheric climate. *Sci. China Ser. D Earth Sci.* 52, 1679–1693.
- Zhu, Z., Li, Y., Xue, C., Han, L., 2011. Changing tendency of precipitation in permafrost regions along Qinghai-Tibet Railway during last thirty years. *J. Glaciol. Geocryol.* 33, 846–850.
- Zou, D., Zhao, L., Sheng, Y., Chen, J., Hu, G., Wu, T., Wu, J., Xie, C., Wu, X., Pang, Q., Wang, W., Du, E., Li, W., Liu, G., Li, J., Qin, Y., Qiao, Y., Wang, Z., Shi, J., Cheng, G., 2017. A new map of permafrost distribution on the Tibetan Plateau. *Cryosphere* 11, 2527–2542.